Published in Journal of Quantum Electronics (IEEE) 38, issue 6, 533-546, 2002
which should be used for any reference to this work

Bound-to-Continuum and Two-Phonon Resonance Quantum-Cascade Lasers for High Duty Cycle, High-Temperature Operation

Jérôme Faist, *Member, IEEE*, Daniel Hofstetter, Mattias Beck, Thierry Aellen, Michel Rochat, and Stéphane Blaser

Invited Paper

***Abstract*—Recent advances in quantum-cascade (QC) laser active-region design are reviewed. Based on a rate equation model of the active region, we show why new gain regions based on a two-phonon resonance or a bound-to-continuum transition exhibit significantly better performance than the traditional design based on a three-quantum-well active region. Threshold current densities as low as 3 kA/cm^2 at $T = 300$ K, operation with a peak power of 90 mW at 425 K, single-mode high-power operation up to temperatures above 330 K at $\lambda \approx 16$ μm and continuous wave operation up to $T = 311$ K are demonstrated. QC lasers able to operate at high duty cycles (50%) on a Peltier cooler were used in a demonstration of a 300-MHz free-space optical link between two buildings separated by 350 m.**

***Index Terms*—Intersubband, laser, mid-infrared.**

I. Introduction

A. Quantum Engineering

THE quantum-cascade (QC) laser [1] is one the best examples of a quantum device where fundamental properties, such as the emission wavelength, are not an intrinsic property of the semiconductor but a result of the *design* of the epitaxial layers. Similarly, the population inversion is not caused by some intrinsic physical property of the system, but must be designed by a suitable engineering of the wavefunctions. QC lasers have demonstrated operation in a wide wavelength range (3–24 μm). Their applications to optical spectroscopy by a variety of techniques are discussed in a review by Tittel in this issue.

Optimization of the device performance, necessary for these applications, requires an accurate modeling of the electronic and optical processes. At cryogenic temperatures, good agreement has been obtained between computed and measured threshold current densities and slope efficiencies for a large class of devices [2], [3]. In contrast, at 300 K, the predicted value of threshold current density (between 1 and 3 kA/cm^2, depending on whether theoretical or experimental values of the waveguide losses are used) was much lower than the experimental values reported in the literature (between 4.6 and 7 kA/cm^2). Achieving threshold current values closer to the theoretical predictions was crucial to improving the room temperature performances of QC laser devices in order to allow, in particular, continuous wave operation at room temperature.

The authors are with the Institute of Physics, University of Neuchâtel, CH-2000 Neuchâtel, Switzerland (e-mail: Jerome.Faist@unine.ch).

B. Organization of the Paper

This paper is organized as follows. In Section II, the fundamentals of the population inversion between subbands are derived, as well as a model showing the reason for developing new structures. In Section III, results for QC lasers based on a two-phonon resonance are shown for multimode and single-mode operation, including high-duty-cycle operation. Section IV discusses results obtained with the bound-to-continuum approach. Application of these structures for telecommunications is discussed in Section V.

C. History

The history of QC laser research is reviewed in this issue in Capasso's paper. Since the focus of our paper is the analysis of the active region designs, we will quickly review the progress in this area. The first demonstration of QC lasers used the so-called three-quantum-well (3QW) active region [1]. In this design, population inversion is maintained by a combination of an optical phonon resonance between the two lowest states and a diagonal transition between the two laser states. However, the flexibility offered by quantum design of intersubband transitions enabled a number of other active region designs. As shown in Fig. 1, these active regions have been based on the following.

- One quantum well, with the population inversion based on tunneling from the ground state of the quantum well and nonparabolicity [4].
- Two quantum wells, with the population inversion now based on the resonance with the optical phonon [5]–[7].
- A photon-assisted tunneling transition across a barrier, with the population inversion based solely on tunneling [8].
- Transitions between minibands in a superlattice active region. The population inversion now relies on a difference between the phase space to scatter into and out from the lower state of the laser transition [9].

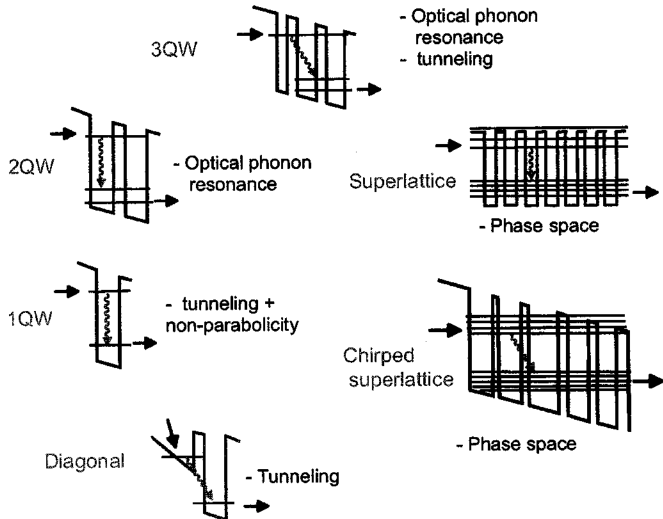

Fig. 1. Various active regions described in the literature. They are based on one quantum well [4], two quantum wells [7], the 3QW active region extensively discussed in the text, photon-assisted tunneling structures [8], doped superlattices [9], and chirped superlattices active regions [11], [12].

- Superlattice of coupled wells, chirped, with no injector. The population inversion also relies on a phase space argument [10].

With the exception of the single-quantum-well active region device and the superlattice of coupled wells, all the other structures have demonstrated operation up to room temperature. Nevertheless, the designs based on three quantum wells and on a superlattice active region are the ones that lead to the most interesting developments. Regarding superlattice active regions, the initial devices, based on *doped* superlattices, demonstrated very high output powers (1 W) but at cryogenic temperatures; in addition, their threshold current density remained prohibitively high [9]. Significant performance improvement was achieved by replacing the doping of the active region by a "chirping" of the superlattice to compensate for the applied electric field [11], [12] or by separating the dopants from the electron reservoir [13]. Another approach has been to alternate p- and n-doping planes, creating a space charge that would compensate for the applied field [14]. Poorer performance was obtained in that device, however, with a maximum operating temperature of $T = 220$ K. Other groups have also demonstrated high performances using chirped superlattice devices [15]–[17].

The extremely short electron lifetime from the lower state enables superlattice active region designs to operate at very long wavelengths reaching $\lambda \approx$17, 19, 21, and finally up to 24 μm [18]–[21]. However, these structures are limited to operating temperatures below 200–240 K. At these long wavelengths, they however demonstrated superior performance as compared to the 3QW designs [22]. In another work laser action on two different emission lines ($\lambda = 7$ and $\lambda = 9$ μm) was demonstrated [23] also based on a chirped superlattice active region. Intersubband lasers with superlattice active regions have also been demonstrated in the GaAs material system [24] and even achieved continuous wave operation at cryogenic temperatures [25].

3QW active region designs have also shown interesting developments. GaAs-based QC devices are particularly attractive because they enable devices based on more than one aluminum content to be used in the active region. Specifically, the insertion of a high aluminum content barrier between the first two quantum wells has been studied [26]. Another attractive possibility is the use of InGaAs in the center of the wells to increase the emission wavelength [27] or to increase the effective conduction-band discontinuity [28].

New designs trying to combine the features of the 3QW active regions and the superlattice active regions are the subject of this article.

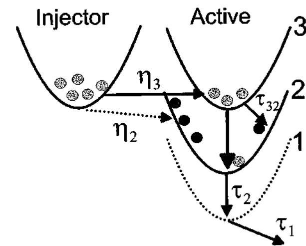

Fig. 2. Schematic description of the relevant levels and injection efficiencies in a cascade laser.

II. Population Inversion Between Subbands

A. Injection Efficiency

In a QC laser, electrons are injected into an upper state (or upper miniband, in the case of superlattice QC lasers [29]) and recombine radiatively to a lower state (or lower miniband). The gain G is proportional to the population inversion Δn between the upper ($n = 3$) and lower ($n = 2$) states. Let us assume, as shown schematically in Fig. 2, that a fraction η_3 of the current is injected into the upper state, and η_2 into the lower state. In this case, G can be written as [30]

$$G = \sigma \Delta n = \sigma \frac{J}{q_0} \left(\tau_3 \eta_3 \left(1 - \frac{\tau_2}{\tau_{32}} \right) - \eta_2 \tau_2 \right) \tag{1}$$

where τ_3, τ_2 are the (total) lifetimes, τ_{32} is the intersubband scattering time between the states $n = 3$ and $n = 2$, and σ is the transition cross section [2]. In the case of QC lasers based on a superlattice active region, (1) can still be applied with the $n = 3$ state being the lower state of the upper miniband and $n = 2$ the upper state of the lowest miniband. Equation (1) shows clearly the strong dependence of the gain on both injection efficiencies and the ratio of the lifetimes: one must design a structure which maximizes the difference $\eta_3\tau_3 - \eta_2\tau_2$ and minimizes the ratio τ_2/τ_{32}.

As discussed above, high-performance room temperature QC lasers have been demonstrated so far using either 3QW active region [2] or a superlattice, which for the best performance can be "chirped" to compensate for the applied field [11], [29]. In both cases, the necessity to confine the upper state of the active region requires the laser to be separated into an active region followed by an injection/relaxation region.

Although (1) has limited predictive power because the critical parameters (injection efficiencies and lower state lifetimes) are not easily computed or measured, it qualitatively explains the different strategies these two designs have employed to achieve

low-threshold room-temperature performance: the 3QW maximizes the first term ($\eta_3\tau_3$), while the superlattice designs minimize the second term ($\eta_2\tau_2$).

In the 3QW active region devices, a large value of η_3 is achieved by the penetration of the $n = 3$ state into the injection barrier [2], [31] that enhances the coupling to the $n = 3$ state while minimizing the coupling to the lower states of the active region (i.e., $\eta_3 \gg \eta_2$). The extraction of the electrons from the $n = 2$ state is enhanced by the resonant nature of the optical phonon transition between the $n = 2$ and $n = 1$ states [2], implying a short value of τ_{21} ($\tau_{21} \approx 0.2$–0.4 ps). However, in such a design, the small value of τ_{21} is misleading because, ultimately, the population of the $n = 1$ state (and also $n = 2$) is extracted into the injection/relaxation region by a tunneling process.

B. Electron Extraction Bottleneck

The value of the tunneling time τ_{esc} is difficult to estimate accurately. Experimental values obtained in QC structures yield $\tau_{\text{esc}} = 2$–3 ps [4], [32], much larger than τ_{21} and the value (0.2 ps) computed assuming the injection region behaves as a continuum.

A model of the room-temperature electron kinetics in the active region, that included optical phonon emission and absorption from all points in k-space (see Fig. 3) of the active region subbands, demonstrated that this long escape time creates an effective bottleneck effect. In this model, the electrons are interacting with a bath of optical phonons in thermal equilibrium at a temperature T. Since we are neglecting electron–electron interactions, the electron may gain or lose energy only in quanta of the optical phonon energy. Fig. 3 schematically shows this model in a case where the transition energy corresponds to the emission of four optical phonons. We label the available states by two indices (i, j), where i labels the state number and j the position in the ladder of energies. $j = 0$ corresponds to the energy of the electron injection, $j = 1$ to the emission of one optical phonon, and so on. For an active region containing N states (with N being the upper laser state), the rate equation for the lower states (i, j) (with $i < N$) reads

$$\frac{dn_{i,j}}{dt} = \sum_{k=1}^{N-1}\left(\frac{n_{k,j-1}}{\tau_{ik}^{e}} + \frac{n_{k,j+1}}{\tau_{ik}^{a}}\right) + \delta_{j,1}\frac{n_{N,0}}{\tau_{Ni}^{e}} + \delta_{j,-1}\frac{n_{N,0}}{\tau_{Ni}^{a}} - n_{i,j} \cdot \left[\sum_{k=1}^{N-1}\left(\frac{1}{\tau_{ik}^{a}} + \frac{1}{\tau_{ik}^{e}}\right) + \frac{1}{\tau_{\text{esc}}} + \delta_{j,1}\frac{1}{\tau_{Ni}^{a}} + \delta_{j,-1}\frac{1}{\tau_{Ni}^{e}}\right] \quad (2)$$

where $\delta_{j,\pm1}$ is the Kroenecker delta. We assume that a cool electron distribution is injected in the upper laser level. Therefore, all the electrons are concentrated in $j = 0$ in the upper level N. The rate equation for that state reads

$$\frac{dn_{N,0}}{dt} = \frac{J}{q_0} + \sum_{k=1}^{N-1}\frac{n_{k,1}}{\tau_{N,k}^{a}} - n_{N,0}\sum_{k=1}^{N-1}\left(\frac{1}{\tau_{N,k}^{e}} + \frac{1}{\tau_{N,k}^{a}}\right). \quad (3)$$

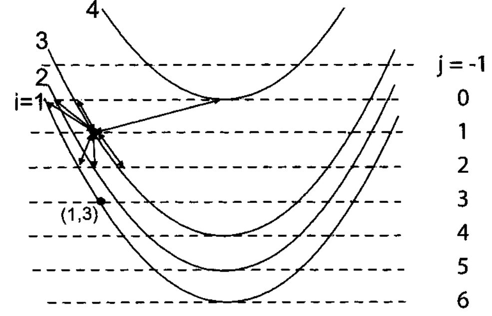

Fig. 3. Schematic description of the rate equation model in k-space for an active region for a device based on a two-phonon resonance.

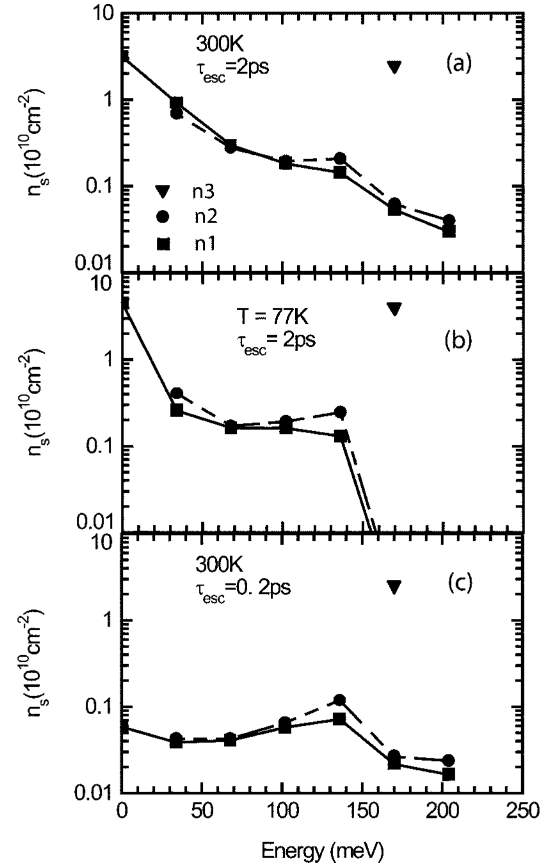

Fig. 4. Electron sheet density (in units of 10^{10} cm^{-2}) in the three relevant subbands of the active region of a 3QW structure, as a function of energy. The computed lifetimes correspond to an InGaAs–AlInAs laser operating at $\lambda = 9$–10 μm [31], [33], under an injected current $J_0 = 5$ kA/cm^2. $E = 0$ is at the bottom of the lowest subband. (a) $T = 300$ K, $\tau_{\text{esc}} = 2$ ps. (b) $T = 77$ K, $\tau_{\text{esc}} = 2$ ps. (c) (a) $T = 300$ K, $\tau_{\text{esc}} = 0.2$ ps.

Solving (2) and (3) for a given injection current and temperature yields the densities at each relevant point of k-space. The result of such a computation is shown in Fig. 4. This model nicely demonstrates the "bottleneck" effect of the long tunneling escape time τ_{esc}. In Fig. 4, the sheet electron density $n_{i,j}$ is reported, for each subband, as a function of kinetic energy E in the subband ($E = j * \hbar\omega_{LO}$). The total sheet density in each subband n_i may then be computed by summing over j. At room temperature ($T = 300$ K), the ratio of lower to upper state population is $n_2/n_3 = 0.59$ [see Fig. 4(a)], a value much larger than the one anticipated by considering the lifetimes $\tau_2/\tau_{32} = 0.2$.

Even at cryogenic temperature ($T = 77$ K), this ratio $n_2/n_3 = 0.26$ [see Fig. 4(b)] is larger than the one predicted from the lifetimes $\tau_2/\tau_{32} = 0.1$. As expected, if the escape lifetime is set to a short value $\tau_{\rm esc} = 0.2$ ps, the ratio of population is small, even at room temperature: $n_2/n_3 = 0.136$ [see Fig. 4(c)].

The effect of this bottleneck can be expressed as an effective lower state lifetime $\tau_2^{\rm eff}$ such that $n_2/n_3 = \tau_2^{\rm eff}/\tau_{32}$. At $T = 300$ K, we find a value $\tau_2^{\rm eff} = 0.8$ ps.

The situation for electron extraction is significantly different in superlattice active region designs. In those designs, the injection efficiency in the lower state η_2 is made small by a phase space argument: the $n = 2$ state is only one of a manifold of lower states forming the lower miniband and thus injection into this state is unlikely. Similarly, $\tau_2^{\rm eff}$ is expected to be small ($\tau_2 \cong 0.2$ ps) through very efficient intrasubband scattering. In addition, no bottleneck problems are foreseen, since transport in the lower miniband provides efficient electron extraction. However, η_3 is not expected to be as large as in the 3QW case, since electron injection is not achieved through resonant tunneling [29].

These considerations are supported by the experimental evidence. Resonant tunneling effects have been observed in the 3QW active region up to room temperature, as expected for large values of η_3 [31], [34]. The possibility of achieving multi-wavelength operation [23] in superlattice active region designs supports the idea that at least some of the electron injection into the superlattice active region occurs through capture and is therefore less efficient. The high lower state extraction efficiency of superlattice designs is proven by their ability to operate at very high injection current densities (up to 30 kA/cm^2) [29].

Similar conclusions on injection efficiency are obtained from a theoretical approach where the injection process is modeled as an intersubband scattering. A crude computation of the injection efficiency can then be performed by evaluating the form factors

$$I_{ij}(q_{\rm if}) = \iint \phi_i(z)\phi_f(z)e^{-q_{\rm if}|z-z'|}\phi_i(z')\phi_f(z')\,dz\,dz' \quad (4)$$

that are central to most intersubband processes, such as optical phonon scattering, electron–electron scattering, and interface roughness scattering [35]. The injection efficiency η_j into the states $n = j$ may then be computed for various designs as

$$\eta_j = \frac{I_{ij}}{\sum_k I_{ik}} \quad (5)$$

where I_{ik} is evaluated between the injector state $n = i$ and the various states of the active region. Equation (5) has been evaluated for a 3QW design [33], where $\eta_3 = 0.87$ and $\eta_2 = 0.07$ and for a chirped superlattice design [11] with $\eta_3 = 0.76$ and $\eta_2 = 0.04$. This model, however, tends to overestimate the injection efficiencies since it does not include dephasing.

C. New Designs

We propose here designs that attempt to take advantage of the resonant tunneling injection feature of the 3QW design and the electron extraction efficiency of the superlattice design. Both designs, shown schematically in Fig. 5, share the same upper laser level geometry but differ by their extraction mechanism.

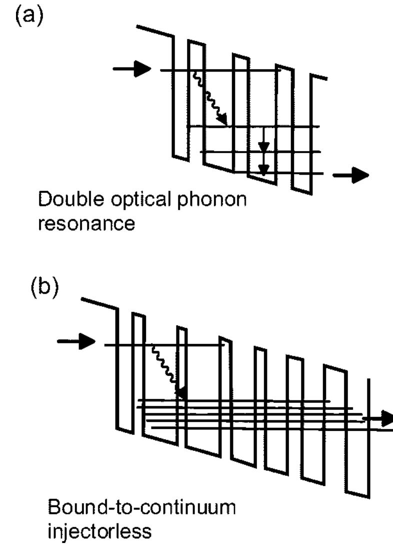

Fig. 5. New designs discussed in this article. The active regions is based on bound-to-continuum transition [30] or two phonon resonances [36].

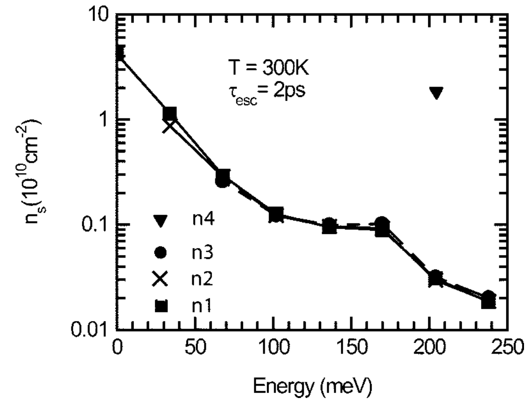

Fig. 6. Electron distribution in the three four relevant subbands of the active region of a four quantum well structure, as a function of energy. The computed lifetimes correspond to an InGaAs–AlInAs laser operating at $\lambda = 9$ μm [37], under an injected current $J_0 = 3$ kA/cm^2 at $T = 300$ K. $E = 0$ is at the bottom of the lowest subband and the escape time is $\tau_{\rm esc} = 2$ ps. The 300 K emission, respectively absorption lifetimes from the active region states ($n = 4$ is the upper laser level) are (in ps) $\tau_{43}^e = 1.88$, $\tau_{43}^a = 9.3$, $\tau_{42}^e = 1.92$, $\tau_{42}^a = 8.5$ps, $\tau_{41}^e = 2.51$, $\tau_{41}^a = 11.5$, $\tau_{32}^e = 0.73$, $\tau_{32}^a = 3.8$, $\tau_{31}^e = 0.23$, $\tau_{31}^a = 2.3$, $\tau_{21}^e = 0.28$, $\tau_{21}^a = 2.7$. The lifetime for intrasubband processes are $\tau^{\rm em} = 0.14$ ps for emission and $\tau^{\rm abs} = 0.55$ ps for absorption of optical phonon.

In a bound-to-continuum design, the radiative transition occurs between an isolated state and a miniband providing an efficient extraction mechanism (see Fig. 5). In the two-phonon resonance design, the extraction is obtained by a ladder of three states separated by an optical phonon each (Fig. 5). According to our computation, the addition of this extra level decreases significantly the population of the lower state. We computed the electron distribution in the subbands of such a structure, described in the next paragraph and emitting at $\lambda \approx 9$ μm. The result of these calculations, as well as the value of the intersubband scattering times used, are shown in Fig. 6 and its caption, respectively. A reduced lower state population now yields a more favorable ratio of lower to upper state: $n_3/n_4 = 0.35$ at $T = 300$ K. The corresponding effective lower state lifetime has now decreased to $\tau_3^{\rm eff} = 0.192$ ps.

III. Experiments: Two-Phonon Resonance Active Region

A. Long Wavelength (9 μm) Devices

Up to the active region, growth of this material was based on molecular beam epitaxy (MBE) of lattice matched InGaAs/InAlAs layers on top of an n-doped InP (Si, $n = 2 \times 10^{17}$ cm^{-3}) substrate. After the waveguide core with the active region, an epitaxial over-growth by metal-organic vapor phase epitaxy (MOVPE) of the InP top cladding and contact layers completed the growth. The MBE growth process started with the lower waveguide layer (InGaAs, Si, $n = 6 \times 10^{16}$ cm^{-3}, total thickness 0.225 μm), proceeded with an active region (thickness 1.82 μm) and was finished by an upper waveguide layer (InGaAs, Si, 6×10^{16} cm^{-3}, thickness 0.23 μm). After thorough cleaning of the surface in H_2SO_4, the samples were transferred to an MOVPE system, where the top cladding layer (InP, Si, 1×10^{17} cm^{-3}, thickness 2.5 μm), the contact layer (InP, Si, 7×10^{18} cm^{-3}, thickness 0.85 μm), and the cap layer (InP, Si, 1×10^{19} cm^{-3}, thickness 10 nm) were grown. The gain region, which formed the central part of the waveguide, consisted of 35 periods; these were alternating n-doped funnel injector regions and undoped two phonon resonance active regions. A schematic conduction-band diagram of one period of the active region is shown in Fig. 7. The upper and lower lasing states are the wavefunctions with numbers 4 and 3, respectively. As already mentioned in the preceding paragraph, the active region was composed of four quantum wells, which results in three coupled lower states (levels 1, 2, and 3). Each two of the latter (i.e., level 3 and 2, and level 2 and 1) were separated by one phonon energy. This double-phonon resonance yields a short intersubband electron scattering time (see values in caption of Fig. 6) and, therefore, an efficient extraction of the electrons into the injector region. The upper lasing state exhibits a much longer intersubband electron scattering time of $\tau_{\rm up} = (\tau_{43}^{-1} + \tau_{42}^{-1} + \tau_{41}^{-1})^{-1} = 0.54$ ps (at $T = 300$ K), where the lifetimes contain both emission and absorption processes. The relatively large dipole matrix element $\langle z_{43} \rangle = 3.0$ nm confirms that the lasing transition is mainly a vertical one. Thanks to the thin first well, which reduces the overlap of the injector ground state with the lower lasing state wavefunctions 1, 2, and 3, the injection efficiency was kept similarly high as in the classical 3QW design. Thus, the new design takes advantage of the good properties of both the 3QW design (high injection efficiency) and the superlattice design (short lifetime of the lower lasing state).

Low-temperature ($T = 80$ K) luminescence spectra were taken from a device in which the light was extracted from a 45° wedge polished in the substrate. These spectra, taken for various injection currents, are shown in Fig. 8 along with the calculated transition energies. All the transitions in the active region can easily be identified. Our computations show that the dipole matrix elements between states $4-1$ and $5-1$ are always very small (z_{51}, $z_{41} < 0.1$ nm), regardless of the applied electric field. Peaks related to transitions from level 5 can only be observed in the strong injection regime, as observed experimentally. The computed dipole matrix element z_{42} decreases strongly with applied field, as observed in Fig. 8. In general, the

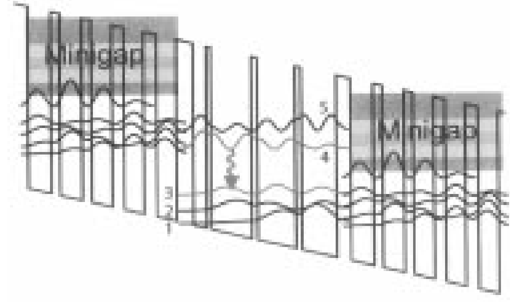

Fig. 7. Schematic band diagram of a two-phonon resonance gain region designed for operation at $\lambda \approx 9$ μm. The layer sequence of the structure, in nanometers, and starting from the injection barrier, is as follows: **4.0**/1.9/**0.7**/5.8/**0.9**/5.7/**0.9**/5.0/**2.2**/3.4/**1.4**/3.3/**1.3**/3.2/**1.5**/3.1/**1.9**/3.0/**2.3**/2.9/**2.5** /2.9/ nm. $In_{0.52}Al_{0.48}As$ barrier layers are in bold, $In_{0.53}Ga_{0.47}As$ well layers are in roman, and n-doped layers (Si 4×10^{17} cm^{-3}) are underlined.

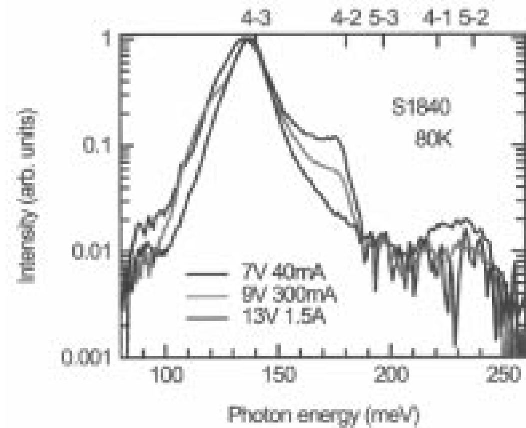

Fig. 8. Low-temperature ($T = 80$ K) luminescence spectra of the active region based on a two-phonon resonance. Calculated transition energies are shown on the top horizontal axis.

luminescence peaks shown in Fig. 8 confirm the location and strength of the respective intersubband transitions.

Fabry–Perot (FP), 28-μm-wide ridge waveguide devices were fabricated using wet chemical etching and Si_3N_4 passivation. For testing, the devices were placed into a Peltier-cooled aluminum box with an anti-reflection coated ZnSe-window (Alpes Lasers SA). Average output power and voltage versus current (L–I–V) curves at temperatures of -30 °C, 0 °C, 30 °C, and 60 °C were measured in this configuration. A pulse length of 40 ns was used with a variable pulse repetition frequency $f_{\rm rep}$ in order to achieve a duty cycle between 1.5% ($f_{\rm rep} = 375$ kHz) and 20% ($f_{\rm rep} = 5$ MHz). For higher duty cycles, we left the repetition frequency constant at 5 MHz and changed the pulse length from 40 to 165 ns. The average output power was measured using a calibrated thermopile detector.

Typical L–I- and I–V-curves of a 3-mm-long device are shown in Fig. 9. The 45-ns-long pulses were produced with a pulse repetition frequency of 333 kHz; this corresponds to a duty cycle of 1.5%. The emitted peak power decreases from 1.6 W at -30 °C to more than 800 mW at 60 °C. The corresponding slope efficiency is 300 mW/A at 30 °C. We observed threshold currents densities of 2.2, 3.6, and 5.6 kA/cm^2 at -30 °C, 30 °C, and 60 °C. The characteristic temperature T_0, which empirically describes the behavior of the threshold current as a function of the temperature, was 214 K.

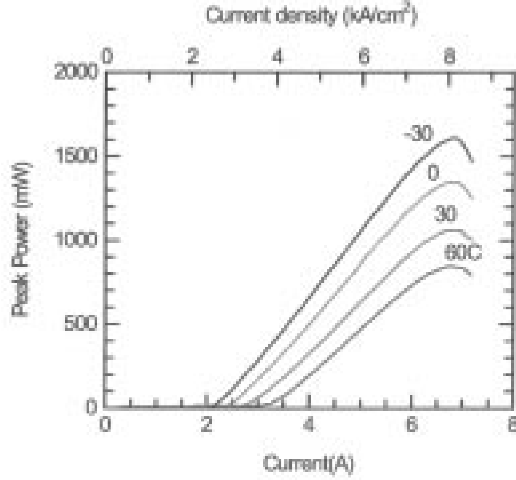

Fig. 9. Pulsed peak power versus injected current characteristics of a 3-mm long and 28-μm wide two-phonon resonance device. The device is driven at a low (1.5%) duty cycle.

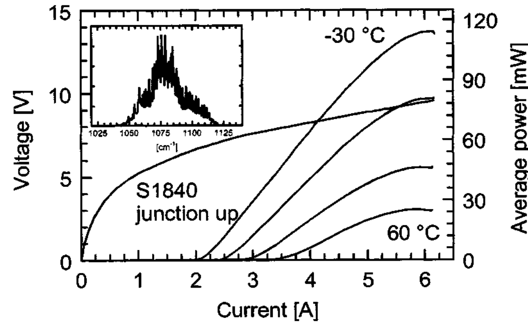

Fig. 10. Pulsed peak power versus injected current characteristics of a 3-mm long and 28-μm wide two-phonon resonance device at high (15.5%) duty cycle.

B. High Duty-Cycle Operation

In Fig. 10, we present a series of L–I–V-curves of the same device (see Fig. 9) but at a high duty cycle. At -30 °C and for 15.5% duty cycle, a maximal average power of 115 mW was seen; the threshold current density under these conditions was on the order of 2.68 kA/cm^2. At 30 °C, the corresponding numbers are 47 mW and 3.72 kA/cm^2; this was already slightly lower than the maximal power of 54 mW at 11.5%. As shown in the inset of Fig. 10, the emission wavelength of this laser was around 1070 cm^{-1}, or 9.3 μm. Because of the vertical transition used, the wavelength did not change at higher current injection currents.

Similar experiments as shown above for S1840 were made with the lower doped, junction-down mounted sample S1850. Due to the slightly lower doping in the active region, it showed lower output powers and slope efficiencies; however, the threshold current density was somewhat better than the one of S1840. At low duty cycle, a 3-mm long and 28-μm-wide laser exhibited 147 mW/A at -30 °C (j_{th} = 2.44 kA/cm^2) and 120 mW/A at 30 °C (j_{th} = 3.0 kA/cm^2). Because of the copper heatsink being somewhat longer than the laser cavity, the lower slope efficiency might be partly due to a shadowing effect. A T_0 value of 226 K was calculated for this device.

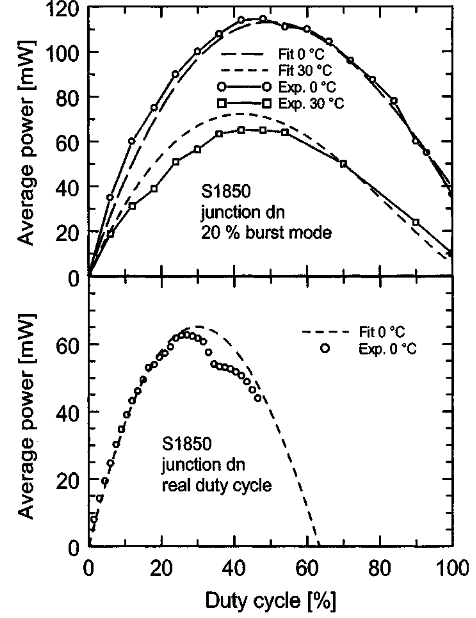

Fig. 11. Thermal rollover average power versus duty cycle-curves of the device S1850 at 0 °C and at 30 °C for burst mode (top) and for normal pulsed operation (bottom). A burst duty cycle of 20% and a repetition frequency of 10 kHz were used for this experiment. The dashed lines are theoretical fits using a thermal resistance value of 2.9 K/W (burst) and 5.67 K/W (normal).

If such a device is operated at high duty cycle, the Peltier-cooler, which can dissipate 20 W of thermal power, can reach the limit of its capabilities. This is why we tested our lasers in burst mode as well.

In Fig. 11, we compare the device performance of S1850 at high duty cycle in normal pulsed operation and in burst mode operation. In 20% burst mode, the thermal load on the Peltier cooler is reduced considerably, because the laser is in "normal" pulsed mode during 20 ms only. This short period is followed by a period of 80 ms during which the device remains unbiased. As shown in the upper part of Fig. 11, the duty cycle within the burst could be cranked up to a value of 100% (which corresponds to 20% "real" pulsed operation) for both 0 °C and 30 °C. The maximal average power during the burst was 112 mW for 0 °C and 60 mW for 30 °C. At 100% duty cycle within the burst, average powers of 36 and 10 mW, were obtained for 0 °C and 30 °C, respectively.

As with device S1840, we calculated the thermal conductance of the laser and found a value of 410 W/cm^{2}K^{-1} ($R_{th} =$ 2.9 K/W). The lower half of Fig. 11 shows the measurements at real pulsed operation. Here, the maximal thermal roll-over output power for 0 °C (66.5 mW) was reached already 27% duty cycle. The dashed line corresponds to the simulated curve using a total thermal resistance value of $R_{\rm th} = 5.67$ K/W. The thermal resistance difference between regular pulsed operation and burst mode corresponds to the thermal resistance of the laser submount. It is obvious that the latter still contributes a considerable fraction, almost 50%, of the total thermal resistance. In addition, the deviation of the experimental points from the theoretical curve for a 40% duty cycle is probably an indication of an early device aging process.

C. Short Wavelength (5 μm) Devices

Spectroscopy applications also require high performance devices in the 5-μm wavelength range. To enable the realization of a two-phonon resonance active region while minimizing the carrier overflow required the use of a material with a larger conduction band discontinuity. We used strain-compensated $In_{0.60}Ga_{0.4}As$–$In_{0.44}Al_{0.56}As$ that provides a barrier height considerably larger (620 meV instead of 520 meV) than the unstrained material. This efficiently reduced electron tunneling from the upper lasing state into the continuum [36].

Spectroscopy applications also require single mode device operation with accurate wavelength control. This is achieved using a distributed feedback (DFB) structure in which a grating etched in the active region of the device provides a highly wavelength selective feedback mechanism. A technique that provides a large grating coupling strength combined with a relatively simple processing was used [38]. In this approach, current injection into the grating layer was accomplished laterally through narrow metal stripes on the shoulders of the waveguide. This waveguide design has the advantages of being simple (no epitaxial re-growth), offering a strong coupling coefficient, and, finally, resulting in small absorption losses. Fabrication of these devices relied on MBE of strain-compensated $In_{0.60}Ga_{0.4}As/In_{0.44}Al_{0.56}As$ layers on top of an n-doped InP (Si, 2×10^{17} cm^{-3}) substrate. The growth process started with the lower waveguide layers ($In_{0.53}Ga_{0.47}As$, Si, 6×10^{16} cm^{-3}, thickness 0.34 μm), proceeded with a gain region (Si, thickness 1.43 μm) and was finished by a thicker set of upper waveguide layers ($In_{0.53}Ga_{0.47}As$, Si, 6×10^{16} cm^{-3}, thickness 0.5 μm) and a highly n-doped cap layer ($In_{0.53}Ga_{0.47}As$, Si, 2×10^{18} cm^{-3}, thickness 0.4 μm) on top. This cap layer was also the host layer for the grating, as reported earlier [33], [38]. The central portion of the waveguide consisted of 28 periods; each one of the latter contained an active region and an injector region, separated by an injection- and an exit barrier.

We did not observe any detrimental effect from the use of strain-compensated material. On the contrary, because of the lower effective mass cause by the larger indium content in the wells, all wells can be made somewhat thicker, which has a positive effect on the interfacial roughness scattering. This is consistent with the relatively narrow linewidth of the luminescence peak measured at 4 K ($h\nu = 244$ meV, $\Delta E = 11$ meV) and at 300 K ($h\nu = 233$ meV, $\Delta E = 25$ meV). As shown in Fig. 12, the general philosophy of the design is the same as that for the one operating at $\lambda = 9$ μm. These devices were fabricated into single frequency distributed feedback structures for chemical sensing applications. The fabrication process started by holographically defining a grating with an 0.825 μm period ($n_{\rm eff} = 3.21$), and wet chemical etching of the grating to a depth of 100 nm in a $H_3PO_4/H_2O_2/H_2O$ solution ($4:1:10$, etch rate 800 nm/min). We used a 488-nm Ar-ion laser and a 90° corner reflector mounted on a rotational stage for the grating exposure. 44-μm-wide ridges were etched by wet chemical etching; the electrical insulation was provided by a Si_3N_4 layer. All devices were mounted ridge side up on copper heatsinks, and then placed into the Peltier-cooled box.

Typical L–I- and I–V-curves of a 44-μm wide and 3-mm long device are shown in Fig. 13 for a duty cycle of 1.5%.

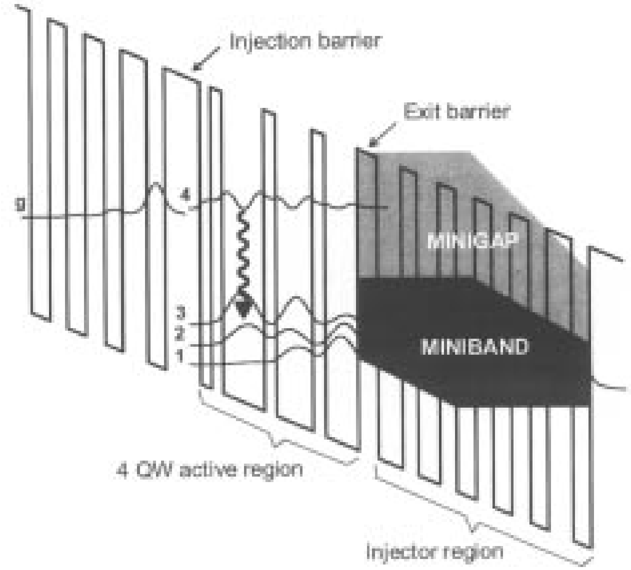

Fig. 12. Schematic conduction band diagram of a portion of the active region and moduli squared of the relevant wavefunctions of a 5.3-μm QC laser with a 4QW active region. An electric field of 7.5×10^4 V/m was applied to align the structure. The $In_{0.60}Ga_{0.4}As/In_{0.44}Al_{0.56}As$ layer sequence of one period of the active region, starting from the injection barrier is as follows: **42**/13/**14**/50/**14**/44/**15**/39/**24**/29/**19**/26/**20**/23/**21**/22/**23**/21/**30**/21. Thicknesses are in *Angstrom*, $In_{0.44}Al_{0.56}As$ barrier layers in bold, $In_{0.60}Ga_{0.4}As$ QW layers are in roman, doped layers (Si, 4×10^{17} cm^{-3}) are underlined.

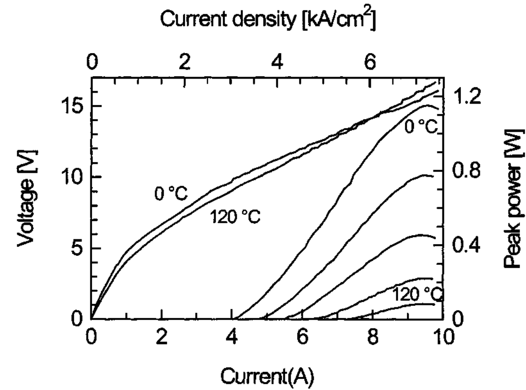

Fig. 13. L–I- and I–V-curves of a 44 μmm wide and 3 mm long QC DFB laser at a wavelength of 5.3 μm. The curves were measured at a duty cycle of 1.5% and at 5 different temperatures between 0 °C and 120 °C.

The 45-ns-long pulses were produced at a pulse repetition frequency of 333 kHz; this corresponds to a duty cycle of 1.5%. The emitted peak power is 1.15 W at 0 °C and 92 mW at 120 °C. The measured slope efficiencies are 247 mW/A at 0 °C and 45 mW/A at 120 °C. We observed threshold currents of 4.1 A at 0 °C and 7.4 A at 120 °C; these values are equivalent to threshold current densities of 3.1 kA/cm^2 and 5.6 kA/cm^2, at the respective temperatures. The characteristic temperature T_0, which empirically describes the behavior of the threshold current as a function of the temperature, was 203 K. As a comparison, we also fabricated FP lasers from the same material, using the same lateral current injection scheme and an identical geometry. For those multimode lasers, we achieved even higher peak powers of 1.76 W at 0 °C ($dP/dI = 311$ mW/A, $j_{th} = 3$

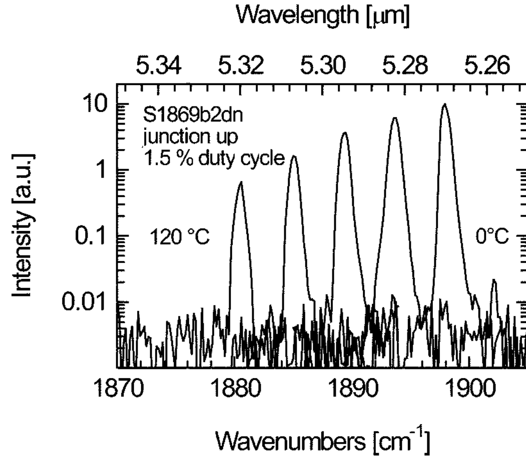

Fig. 14. Emission spectra of a 44-μm wide and 3-mm long QC DFB laser at a wavelength of 5.3 μm. The spectra were collected at the same five temperatures as the L–I–V-curves of Fig. 13 and at the thermal roll-over point for each temperature.

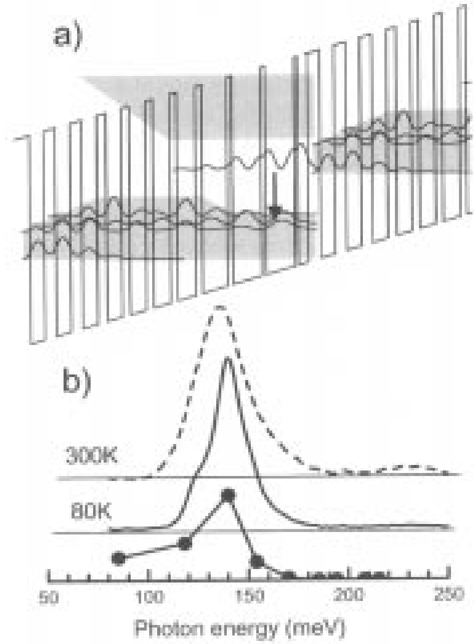

Fig. 15. (a) Schematic conduction band diagram of one stage of the structure under an applied electric field of $3.5 \cdot 10^4$ V/cm. The moduli squared of the relevant wavefunctions are shown. The layer sequence of one period of structure, in nanometers, left to right and starting from the injection barrier is **4.0**/2.0/**0.7**/6.0/**0.9**/5.9/**1.0**/5.2/**1.2**/3.8/**1.2**/3.2/**1.2**/3.2/**1.6**/3.1/**1.9**/3.1/**2.2**/3.0/**2.2**/2.9 where $In_{0.52}Al_{0.48}As$ layers are in bold, $In_{0.53}Ga_{0.47}As$ in Roman and underlined number correspond to doped layer with Si to $N_d = 3 \times 10^{17}$ cm^{-3}. (b) luminescence spectrum of the active region at 300 and 80 K, as indicated. The applied bias is 9 V. Lower curve: computed oscillator strength of the various transitions from the upper state.

kA/cm^2) and 0.83 W at 60 °C ($dP/dI = 258$ mW/A, $j_{th} = 5.4$ kA/cm^2). T_0 was 190 K comparably high as for the DFB lasers. The excellent performance of both DFB and FP devices demonstrates that lateral current injection with or without surface gratings is a very effective technique for high-power QC lasers.

Spectral measurements were performed by a 0.3-m focal length grating spectrometer. In Fig. 14, we present the emission spectra measured at the thermal roll-over point for five representative temperatures between 0 °C and 120 °C. The same pulse lengths and repetition rates as in Fig. 13 were used for this experiment. The single lasing mode tunes linearly with temperature from 1898 cm^{-1} at 0 °C to 1881 cm^{-1} at 120 °C. We thus obtained a temperature tuning rate of $\Delta k/\Delta T = -0.145$ cm^{-1}/K. The side-mode suppression ratio (SMSR) decreases from 30 dB at 0 °C to 20 dB at 120 °C due to the limited signal over noise of our measurement setup. The full-width at half-maximum linewidth of the emission peaks is on the order of 0.75 cm^{-1} for all investigated temperatures. It is obvious that thermal chirping dictates this linewidth, as outlined in reference [39]. For this reason, we made experiments with a reduced pulse length (down to 20 ns) and found a linewidth on the order of 0.15 cm^{-1}, limited by the spectral resolution of our spectrometer.

IV. Bound-to-Continuum Active Regions

A. $\lambda \approx 9$ μm Design

Besides the two-phonon resonance approach, the bound-to-continuum approach provides another route for maintaining a high population inversion and low-threshold current densities even at high temperatures. In this design, shown schematically in Fig. 15, the active region spans the whole period and consists of a chirped superlattice presenting a tilted lower miniband whose width is maximum in the center and decreases on both sides close to the injection barriers. The upper state is created in the first minigap by a small well adjacent to the injection barrier. Its wavefunction has a maximum close to the injection barrier and decreases smoothly in the active region. This upper state is well separated from the higher-lying states of the superlattice, lying in its first minigap. It therefore does not need to be confined by separating the structure into an active region and an injection/relaxation region. Because of this large energy separation (60 meV), the injection efficiency η_3 is not reduced by electron injection into higher energy states of the superlattice [40], [41]. In addition, this configuration of the wavefunction should enable an injection efficiency comparable to the one of the 3QW design. The computed injection efficiencies using equation (5) are $\eta_3 = 0.78$ and $\eta_3 = 0.038$. These values are closer to the ones of the chirped superlattice than the 3QW design. However, we believe that it is due to a limitation of our model that does not include the broadening, and, as such, will always describe the coupling between the injector wavefunction and the upper laser state as a coherent one, i.e., the wavefunction of the upper laser state and the ground state of the injector split to form a doublet. In reality, the broadening of the states by interface roughness prevents the observation of this doublet in the intersubband luminescence spectra and, therefore, tunneling between the injector and the upper laser state occurs mainly sequentially.

The structure is grown by MBE using InGaAs and AlInAs alloys lattice-matched on an InP substrate. It consists of a 35-period active region embedded in an optical waveguide formed on one side by the substrate and on the other by an InP top cladding grown by metal organic chemical vapor deposition. Good agreement between the electroluminescence spectrum and the computed matrix elements is found, as shown in Fig. 15. Constructive interference effects [42] can be expected to appear in the emission spectra and will be discussed elsewhere.

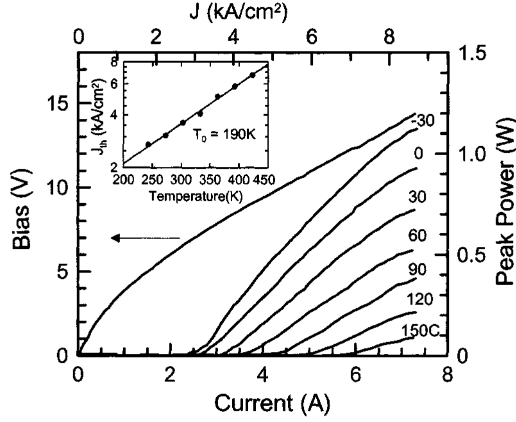

Fig. 16. Peak optical output power versus injected current in pulsed mode at a duty cycle of 1.5% at various temperatures. Inset: Threshold current density as a function of temperature.

The devices were mounted junction-side-up onto a copper sub-mount. Fig. 16 shows the pulsed (1.5% duty cycle) peak optical power from a single facet versus drive current for various temperatures for a 3-mm-long and 28-μm-wide device. Knowing the duty cycle, the peak power was extrapolated from the measurement of the average power with a thermopile power-meter. The device operates at a wavelength of $\lambda = 9.1$ μm. The slope efficiency is $dP/dI = 200$ mW/A at $T = 30$ °C, with a maximum power of 700 mW at this temperature. Peak powers above 1 Watt are achieved at $T = -30$ °C. The small increase in differential resistance at high current could be an indication of a resonant tunneling effect that limits operation with a high injection efficiency to a maximum current density of about 9 kA/cm^2. The high-temperature performance is excellent, with a peak power of 90 mW measured at the maximum operation temperature of 150 °C. In the inset of Fig. 16, the threshold current density $J_{\rm th}$ is plotted as a function of temperature. The data between ≈270 K and 420 K can be described by the usual exponential behavior $J \sim \exp(T/T_0)$ with a value of $T_0 \cong 190$ K. These devices have been also tested at 30 °C with a 6.5% duty cycle, with a maximum average output power of 25 mW.

B. Long Wavelength Bound-to-Continuum Designs

There has been a large effort to develop such devices for even longer wavelengths. These sources would be especially valuable for the detection of large organic hydrocarbon molecules like the benzene, toluene, and xylene (BTX) compounds in the 12–16-μm region or for radio-astronomy as local oscillators in heterodyne detectors.

One of the key problems in the design of long wavelength QC laser is to maintain a large population inversion even at high temperatures. Everything else remaining the same, the decrease of the upper state lifetime with photon energy will decrease this population inversion, as is apparent from the simulations shown in the theoretical part of this paper. Because the "bound-to-continuum" design [30] combines the miniband extraction from the lower state with efficient resonant tunneling injection into the upper state, this approach is very well suited for long wavelength lasers. As shown schematically in Fig. 17(a), the active region of our bound-to-continuum structure spans the whole period and

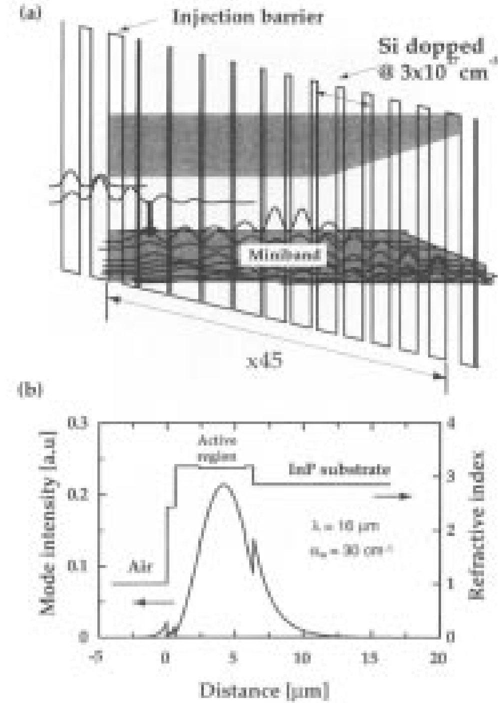

Fig. 17. (a) Schematic conduction band diagram of one stage of the structure under an applied electric field of 2.1×10^4 Vcm^{-1}. The moduli squared of the relevant wavefunctions are shown. The layer sequence of one period of structure, in nanometers, left to right and starting from the injection barrier is **3.3**/3.2/**0.5**/6.5/**0.6**/6.6/**0.7**/6.3/**0.8**/5.8/**1.0**/4.6/**1.2**/4.4/**1.4**/4.4/**1.7**/4.2/**2.0**/4.1/**2.2**/4.0 where $In_{0.52}Al_{0.48}As$ layers are in bold, $In_{0.53}Ga_{0.47}As$ in Roman and underlined number correspond doped regions Si, 3×10^{17} cm^{-3}. (b) Intensity profile and refractive index of the mode for $\lambda = 16$ μm.

exhibits qualitatively the same features as the one made for $\lambda \approx 9$ μm (see Fig. 15). The upper state is created in the first minigap by a small well adjacent to the injection barrier. Its wavefunction has a maximum close to the injection barrier and decreases smoothly in the active region. The computed upper state lifetime $\tau_{\rm up} = 0.68$ ps, is longer than the value ($\tau_{\rm up} = 0.55$) computed for a chirped superlattice emitting at $\lambda = 17\mu$m [18]. This is due to the slightly diagonal nature of the laser transition which leads to a reduced overlap of the upper and lower state wavefunctions, as is apparent from Fig. 17 and leads to a further improved ratio of upper to lower state lifetimes.

In a bound-to-continuum design, the oscillator strength is not concentrated in a single transition, as is the case for a symmetric superlattice but is instead "spread" over two or three states spanning an energy range of ≈ 20 meV. This is in principle a disadvantage of this design because the peak gain is, in a simplified atomistic picture, inversely proportional to the linewidth of the transition. However, this is not a problem anymore for devices optimized for room temperature operation as the intersubband transitions, in designs based on multiquantum-well active region, are anyway collision-broadened to a width of 15–25 meV. On the other hand, this broad gain curves enables the fabrication of single frequency devices over a wide frequency range (≈ 40 cm^{-1} in our case) from a single epitaxial layer.

Because of the reduced overlap between the upper and lower laser state wavefunctions, the equivalent dipole matrix element of the laser transition (averaged over the transitions to the two

upper states of the lower miniband) is $z = 4.0$ nm, lower than the value obtained for a chirped superlattice sample $z = 5.0$ nm.

In the previous work [29], the surface plasmon waveguide [43] was chosen for its ability to achieve simultaneously high overlap factor and a reasonable thickness of grown epitaxial material. However, the experimental value of the waveguide losses of these surface plasmon waveguides was usually found to be significantly higher than the computed one. In our devices, we choose instead waveguides that rely on dielectric confinement by a low-doped InP substrate on one side and air on the other [33] similar to the ones used in the $\lambda \approx 5$ μm DFB devices demonstrated above. The computed refractive index and mode profile of our waveguide is displayed in Fig. 17(b). The computed waveguide absorption caused by free carriers is $\alpha = 30$ cm^{-1}, neglecting the contributions from multiphonon processes. Furthermore, this waveguide configuration allows an easy integration of a DFB grating for single-mode operation.

The structure was grown by MBE using InGaAs and AlInAs alloys lattice matched on top of a very low n-doped InP substrate (Si, $n = 1 \times 10^{17}$ cm^{-3}) and consists of a 45-period active region embedded in an optical waveguide consisting of two low-doped (Si, $n = 6 \times 10^{16}$ cm^{-3}), InGaAs guiding layers 600- and 1750-nm thick, respectively. Mesa ridge waveguides (50–75 μm wide) were processed using wet chemical etching and a hard-baked resist layer for passivation. Contacts were provided by a Ti–Au metallization (10/400 nm) on the edges of the waveguides. The substrate was then mechanically thinned to 150 μm and a back contact (Ge/Au/Ag/Au, 12/27/50/100 nm) was deposited.

The samples were soldered with indium on a copper heatsink and mounted on the Peltier variable temperature enclosure. The electrical power was provided to the lasers with a commercial pulse generator delivering 25–50-ns-long current pulses at a variable repetition rate up to 5 MHz. The optical output power was directly measured with a calibrated thermopile detector. For spectral measurements, the light was collected using a wide numerical aperture gold-coated parabolic off-axis mirror and sent through a Fourier transform infrared spectrometer in rapid scan mode and finally detected by a liquid-nitrogen cooled MCT detector. Typical L–I curves of a 75-μm-wide and 1.6-mm-long FP device are shown in Fig. 18 for temperatures ranging from -40 °C up to 60 °C. The sample is driven with 25-ns-long current pulses at a duty cycle of 0.67%. At -40 °C, the threshold current density is 6.7 kAcm^{-2} with a maximum average output power 2.8 mW, leading to a peak power of more than 400 mW. At 60 °C, the threshold current density is 10 kAcm^{-2} and the maximum peak output power is measured to be more 150 mW. When increasing the duty cycle, we measure a maximum output power of 5.5 mW at -40 °C at a 3% duty cycle, and still more than 1.2 mW of 60 °C with a duty of 1.5%. The highest duty cycle at which a measurable output power (0.2 mW) was seen at -40 °C was 9.6%. The inset of Fig. 18 is a plot of the threshold current density versus temperature. A fit of the threshold current density dependence on temperature using the usual expression $J = J_0 \exp(T/T_0)$ yields a value of $T_0 = 234$ K.

This FP device has a spectral emission in two distinct wavelength windows covering the $\lambda \approx 16.5$ and $\lambda \approx 15.5$ μm, respectively, separated by a absorption peak related to the two

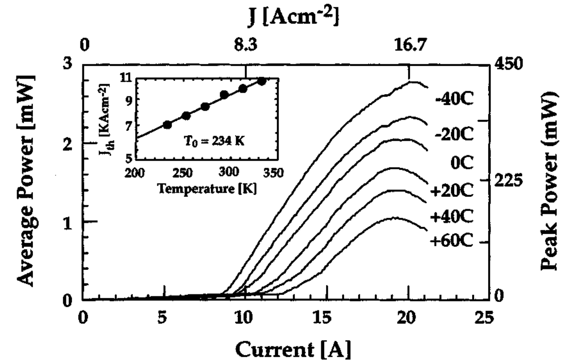

Fig. 18. Peak optical output power versus injected current in pulsed mode at a duty cycle of 0.67% at various temperatures for a device based on a FP cavity. Threshold current density as a function of temperature is shown in the inset.

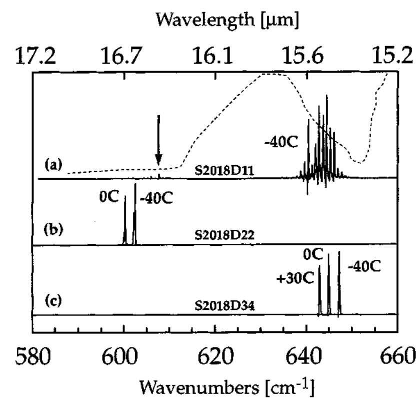

Fig. 19. (a) Emission spectrum of a $\lambda \approx 16$ μm bound-to-continuum device in a FP cavity configuration. An absorption spectrum of an InP substrate is superimposed (dotted lines). Emission spectrum of a device with a DFB grating designed to force the lasing mode at $\lambda \approx 16.5$ μm. Comparison with measured L–I curves, indicate that emission power is single mode up to 0.8 mW. (c) Emission spectrum of a device fitted with a grating designed for $\lambda \approx 15.5$ μm.

phonon absorption in InP [see Fig. 19(a)]. To demonstrate the possibility for our devices to operate in the two spectrally distant regions, we have processed two series of samples with a grating etched into the waveguide. The grating periods were chosen to force a waveguide mode at, respectively, $\lambda \approx 16.5$ and $\lambda \approx 15.5$ μm for samples labeled S2018 D22 and S2018D34. An effective refractive index $n_{\text{eff}} = 3.001$ was used to compute the periodicity.

Fig. 19(b) displays the spectral measurements for the 1.5 mm long and 50 μm wide sample S2018D22. At -40 C, the threshold current density is 7.2 KAcm^{-2}. Up to a peak power of $P = 80$ mW, the emission is single frequency at 602 cm^{-1} ($\lambda = 16.6$ μm). However, side modes appear as the driving current is increased further. At a duty cycle of 1.3%, a maximum (single mode) output power of 2.1 mW has been achieved. With increasing temperature, the peak readshifts up to 600 cm^{-1} ($\lambda = 16.7$ μm) at 0 C. In Fig. 19(c), we have shown the spectral results for sample S2018D34. The sample is 2.250-mm long and 34-μm wide. At -40 °C, the emission peak is centered at 647 cm^{-1} with a threshold current density of 9.0 KAcm^{-2}. Furthermore, as shown in Fig. 19, the emission is single mode, up to a peak output power of $P = 80$ mW. As the temperature is increased, the peak redshifts down to

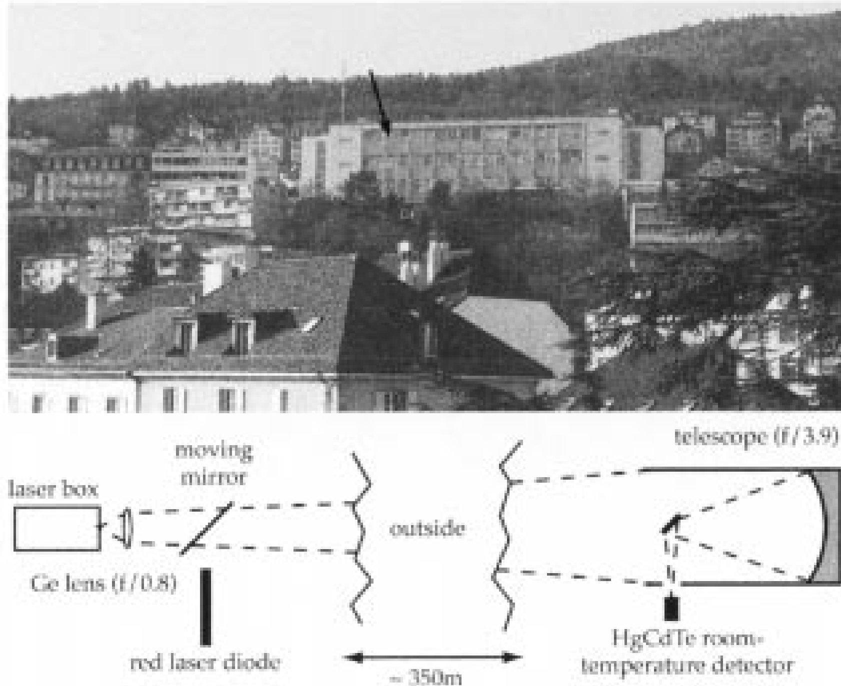

Fig. 20. Top: Photograph showing the building with the receiving electronics in a distance of 350 m (see arrow). Bottom; Systematic representation of the optical data link using a QC laser.

$642\,\mathrm{cm}^{-1}$ at $+30$ C, leading to a temperature tuning $\Delta\nu/\Delta T$ of $0.07\,\mathrm{cm}^{-1}\mathrm{K}^{-1}$. At this temperature, the emission remains singlemode with increasing injected current up to the maximum output power of 0.8 mW at 1.3%.

These results demonstrate the wide tuning possibilities of the bound-to-continuum gain material as we are able to force our devices to lase single mode either at 15.5 or 16.7 μm using a grating etched into the waveguide. These are the longest wavelengths reported for a QC laser at non cryogenic temperatures. These lasers could enable the development of portable BTX sensors based on optical techniques.

V. Telecom Applications

While most potential applications of high performance QC lasers lie in the field of optical spectroscopy, there are also some other interesting areas of use. These include, for example, free-space optical data transmission. In contrast to fiber-optical telecommunications, this technique has the advantage of not requiring additional cables to be buried in the ground. In urban areas where lots of fiber-optical connections already exist, fast free-space optical data links could be quite convenient. QC lasers are very suitable for such applications because their emission wavelength can be chosen in the so-called atmospheric window regions, i.e., around 5 and 10 μm. In addition, the fast internal lifetimes in the device should allow for reasonable modulation frequencies of up to 5–10 GHz [2], [44]. Recently, Martini *et al.* published results of an optical data link using a high-speed modulated, liquid-nitrogen cooled QC laser over a distance of 70 m and under laboratory conditions [45]. They also succeeded in transmitting a video image via a common TV channel frequency. Since this experiment was carried out within the building, one of the main benefits of using QC lasers, namely having an emission wavelength which is barely affected by atmospheric conditions like rain or fog was not yet demonstrated. In addition, the use of liquid nitrogen-cooled equipment on both sides makes the technique less attractive for applications in the field. In order to take full advantage of our existing QC laser technology, we present here an optical data link between two different buildings separated by about 350 m and using a Peltier-cooled QC laser as well as a room temperature HgCdTe detector.

A. Experimental Setup

On the side of the emitter, we used a 3–mm-long 9.3-μm multimode QC laser mounted in a Peltier-cooled, temperature-stabilized aluminum box and an $f/0.8$ Ge lens with a 37.5-mm diameter to collimate the laser beam. The device was held at a temperature of -15 °C, operated at 50% duty cycle and at different pulse repetition frequencies. Using a bias-T, the laser was driven simultaneously at a constant current of 2 A (which corresponds to $0.72 \times I_{th}$) and a 10-W radio frequency signal of up to 350 MHz. On the side of the receiver, we employed a mirror telescope with a diameter of 16 cm and a focal distance of 62.5 cm, a fast room-temperature HgCdTe detector, and a 15-dB small-signal amplifier for the detection of the incoming signal. As schematically shown in Fig. 20, a 1-mW red semiconductor laser pointer was directed collinearly with the QC laser beam to facilitate alignment. In a first stage, we aligned the two laser beams in the lab; then the two beams were bounced off a steering mirror and directed toward the other building where the telescope was installed. The steering mirror could be tilted and rotated by manual micrometer screws. The angular accuracy of this kind of beam steering was about 3×10^{-5} rad. At the distance of the building with the telescope, this corresponded to roughly 1 cm.

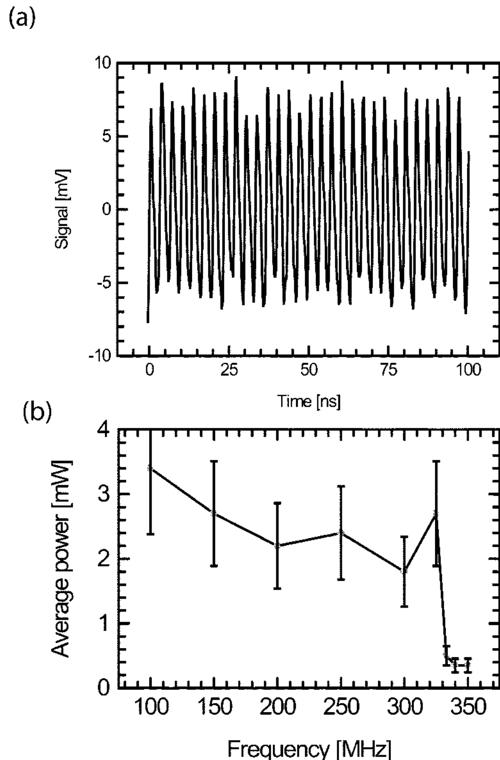

Fig. 21. (a) Stream of pulses after amplification at receiver at a pulse repetition rate of 300 MHz. (b) Transmitted average power on the detector versus modulation frequency.

B. Measurement Results

At a temperature of 258 K and for a 50% duty cycle, the threshold current of the QC laser used for the transmission experiment was 2.7 A ($j_{\rm th} = 3.0$ kA/cm^2). For the maximal injection current of 3.2 A, we observed an average output power of 14 mW. When repeating the power measurement at the other end of the transmission line and at 300 MHz, we still obtained 1.9-mW average power for clear sky conditions; the measured peak power was thus on the order of 3.8 mW. With foggy conditions, the visibility range was evaluated optically to a value below 100 m. However, the average power signal decreased by barely 20% over the 350-m-long transmission range. Since the loss was only on the order of 6 dB, these numbers show clearly the advantage of working at an emission wavelength in an atmospheric window region. As shown in Fig. 21, the typical transmitted signal consisted of a stream of almost sinusoidal pulses with a repetition frequency of up to 330 MHz and a pulse width of 1.5 ns. For 300 MHz, a noise level of roughly 0.25 mW (peak-to-peak value, before amplification) was observed; together with the transmitted peak power mentioned above, this corresponds to a signal to noise ratio of $\approx$15. It should be noted, however, that the detector had a figure of merit of $D^* = 2.2{\times}10^7$ cm$\sqrt{\rm Hz}$/W. From this value, we can calculate the noise equivalent power (NEP) using $D^* = \sqrt{\Delta f A}$/NEP. With $A = 0.625 \times 10^{-2}$ cm^2 being the detector area and $\Delta f =$ 1 GHz the bandwidth of the detector system, we end up with a NEP (amplitude) of 0.11 mW. Within the measurement accuracy, the signal-to-noise ratio is, therefore, dominated by the detectivity of the detector. Improvement in detector technologies based on quantum-well photoconductors (QWIPS) should, therefore, lead to more favorable signal over noise.

In a second experiment, whose result is shown in Fig. 21, we measured the transmitted average power as a function of the pulse repetition rate. It is evident from the figure that the power has a resonance at 325 MHz, and then drops quickly to quite small values. A naive calculation shows that 325 MHz corresponds roughly to the electrical resonance frequency of the laser. The parasitic capacitance defined by the large contact pad area (3 mm $\times$ 0.5 mm) is about 150 pF; together with the resistance of the low-impedance line supplying the current to the laser ($\approx$4 Ω), we end up with an RC time constant of 600 ps. The maximum modulation frequency is, thus, about 250 MHz, in fair agreement with the experimental value.

In a different experimental configuration, we used the QC laser to optically transmit data between two computers. This data link was set up over a distance of 10 m between two optical tables and put together entirely within one laboratory building. On the emitter side, we used the serial port of a first PC and an RS232/TTL signal converter to produce a TTL modulation signal at 115 kbit/s. This signal was used to electrically gate the continuous stream of laser pulses. At the receiver side, the signal was low-pass filtered, amplified, and brought into rectangular shape again with a comparator. After this, we used a timer logic circuit triggered by the positive slopes of the single laser pulses to revert to the initial gate signal, and the final TTL/RS232 converter made the signal compatible to the serial port of a second computer. By this technique, we were able to communicate optically between the two computers at the standard transmission speed of 9.6 kbit/s, and also at the highest possible speed of 115 kbit/s.

VI. Conclusions

We demonstrate in this paper that the two-phonon resonance and the bound-to-continuum approach provide a promising way of addressing the problem of injection and extraction efficiencies to and from the active region of an intersubband QC laser. High performance at room temperature up to very long wavelengths were demonstrated.

The lowering of the threshold current density to values of the order of 3–4 kA/cm^2 at room temperature is especially significant because it potentially allow continuous wave operation of these devices once the heat extraction from the active region has been improved. This was achieved recently [46] by processing a λ =9-μm two-phonon resonance device into a narrow stripe, planarized buried heterostructure geometry in which the gain region was vertically and laterally buried within InP cladding layers grown by metalorganic vapor phase deposition.

This geometry provides a number of advantages. The choice of a buried stripe greatly improves the heat transport by allowing heat flow from all sides of the active region. Additionally, the narrow stripe geometry also decreases the total amount of strain that builds up in a material subjected to a very strong temperature gradient. Indeed, the results from a simulation, using a commercial finite-elements differential equation solver, of both thermal transport and thermally induced stress lead to the same conclusions. A thermal conductance of 820 W/Kcm^2 is pre-

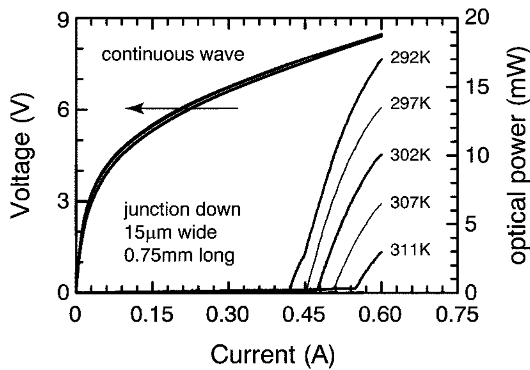

Fig. 22. L–I and I–V characteristics of a buried heterostructure QC laser operating in continuous wave close to room temperature. A maximum continuous wave optical power of 17 mW was achieved with this device.

dicted for a buried, 12-μm-wide, junction-down mounted device, as compared to the calculated value of 510 W/Kcm^2 for a 28 μm wide ridge, junction-down mounted device. Similarly, the maximum thermally induced shear stress that builds up at the edges of the active region decreases from 22 MPa in the ridge device, to 3.6 MPa for the buried structure. L–I and I–V characteristics for a 15-μm wide and 750-μm long structure fabricated using this technology and fitted with high reflectivity ($R \approx 70\%$) mirrors is reported in Fig. 22. This laser emits 17 mW per facet at a drive current of 600 mA at room temperature. This device could be operated up to 311 K with a maximum optical power of 3 mW and a threshold current of 540 mA ($J_{\rm th} = 4.8$ kA/cm^2).

The buried heterostructure geometry used in the latter work could be combined with a DFB grating. Single-mode devices at well-defined wavelengths open new opportunities in very high selectivity sensing applications or free-space optic applications.

ACKNOWLEDGMENT

The authors would like to thank Y. Bonetti, Antoine Müller, D. Körner, and H. Bianchini from Alpes Lasers for their assistance with various parts of this work.

REFERENCES

[1] J. Faist, F. Capasso, D. Sivco, C. Sirtori, A. Hutchinson, and A. Cho, "Quantum cascade laser," *Science*, vol. 264, pp. 553–556, 1994.

[2] J. Faist, F. Capasso, C. Sirtori, D. Sivco, and A. Cho, "Quantum cascade lasers," in *Intersubband Transitions in Quantum Wells: Physics and Device Applications II*, H. Liu and F. Capasso, Eds. New York: Academic, 2000, vol. 66, ch. 1, pp. 1–83.

[3] C. Gmachl, F. Capasso, A. Tredicucci, D. Sivco, R. Köhler, A. Hutchinson, and A. Cho, "Dependence of the device performance on the number of stages in quantum-cascade lasers," *IEEE J. Select. Topics Quantum Electron.*, vol. 5, pp. 808–816, 1999.

[4] J. Faist, F. Capasso, C. Sirtori, D. Sivco, A. Hutchinson, M. Hybertsen, and A. Cho, "Quantum cascade lasers without intersubband population inversion," *Phys. Rev. Lett.*, vol. 76, pp. 411–414, 1996.

[5] J. Faist, F. Capasso, C. Sirtori, D. Sivco, A. Hutchinson, and A. Cho, "Vertical transition quantum cascade laser with Bragg confined excited state," *Appl. Phys. Lett.*, vol. 66, pp. 538–540, 1995.

[6] C. Sirtori, J. Faist, F. Capasso, D. Sivco, A. Hutchinson, S. Chu, and A. Cho, "Continuous wave operation of mid-infrared (7.4–8.6 μm) quantum cascade lasers up to 110 K temperature," *Appl. Phys. Lett.*, vol. 68, pp. 1745–1747, 1996.

[7] C. Sirtori, J. Faist, F. Capasso, D. Sivco, A. Hutchinson, and A. Cho, "Mid-infrared (8.5 μm) semiconductor lasers operating at room temperature," *IEEE Photon. Technol. Lett.*, vol. 9, pp. 294–296, 1997.

[8] J. Faist, F. Capasso, C. Sirtori, D. Sivco, A. Hutchinson, and A. Cho, "Mid-infrared (8.5 μm) semiconductor lasers operating at room temperature," *Nature*, vol. 387, pp. 777–782, 1997.

[9] G. Scamarcio, F. Capasso, C. Sirtori, J. Faist, A. Hutchinson, D. Sivco, and A. Cho, "High-power infrared (8-micrometer wavelength) superlattice lasers," *Science*, vol. 276, pp. 773–776, 1997.

[10] M. Wanke, F. Capasso, C. Gmachl, A. Tredicucci, D. Sivco, A. Hutchinson, S. Chu, and A. Cho, "Injectorless quantum-cascade lasers," *Appl. Phys. Lett.*, vol. 78, pp. 3950–3952, 2001.

[11] A. Tredicucci, F. Capasso, C. Gmachl, D. Sivco, A. Hutchinson, and A. Cho, "High performance interminiband quantum cascade lasers with graded superlattices," *Appl. Phys. Lett.*, vol. 73, pp. 2101–2103, 1998.

[12] A. Tredicucci, F. Capasso, C. Gmachl, D. Sivco, A. Hutchinson, A. Cho, J. Faist, and G. Scamarcio, "High-power inter-miniband lasing in intrinsic superlattices," *Appl. Phys. Lett.*, vol. 72, pp. 2388–2390, 1998.

[13] A. Tredicucci, F. Capasso, C. Gmachl, D. Sivco, A. Hutchinson, and A. Cho, "High-performance quantum cascade lasers with electric-field-free undoped superlattice," *IEEE Photon. Technol. Lett.*, vol. 12, pp. 260–262, 2000.

[14] J. Faist, A. Müller, M. Beck, D. Hofstetter, S. Blaser, U. Oesterle, and M. Ilegems, "A quantum cascade laser based on a n-i-p-i superlattice," *IEEE Photon. Technol. Lett.*, vol. 12, pp. 263–265, 2000.

[15] A. Matlis, S. Slivken, A. Tahraoui, K. Luo, Z. Wu, A. Rybaltowski, C. Jelen, and M. Razeghi, "Low-threshold and high power $\lambda \sim 9.0$ μm quantum cascade lasers operating at room temperature," *Appl. Phys. Lett.*, vol. 77, pp. 1741–1743, 2000.

[16] A. Tahraoui, A. Matlis, S. Slivken, J. Diaz, and M. Razeghi, " High-performance quantum cascade lasers ($\lambda \sim 11$ μm) operating at high temperature ($t \geq 425$ K)," *Appl. Phys. Lett.*, vol. 78, pp. 416–418, 2001.

[17] S. Slivken, A. Matlis, C. Jelen, A. Rybaltowski, J. Diaz, and M. Razeghi, "High-temperature continuous-wave operation of $\lambda = 8\mu$m quantum cascade lasers," *Appl. Phys. Lett.*, vol. 74, pp. 173–175, 1999.

[18] A. Tredicucci, C. Gmachl, F. Capasso, D. Sivco, A. Hutchinson, and A. Cho, "Long wavelength superlattice quantum cascade lasers at $\lambda = 17\mu$m," *Appl. Phys. Lett.*, vol. 74, pp. 638–640, 1999.

[19] A. Tredicucci, C. Gmachl, F. Capasso, A. Hutchinson, D. Sivco, and A. Cho, "Single-mode surface-plasmon laser," *Appl. Phys. Lett.*, vol. 76, pp. 2164–2166, 2000.

[20] A. Tredicucci, C. Gmachl, M. Wanke, F. Capasso, A. Hutchinson, D. Sivco, S. Chu, and A. Cho, "Single-mode surface-plasmon lasers at $\lambda \sim 19\mu$m," *Appl. Phys. Lett.*, vol. 77, pp. 2286–2288, 2000.

[21] R. Colombelli, F. Capasso, C. Gmachl, A. Hutchinson, D. Sivco, A. Tredicucci, M. Wanke, A. Sergent, and A. Cho, "Far-infrared surface-plasmon quantum-cascade lasers at 21.5 μm and 24 μm wavelengths," *Appl. Phys. Lett.*, vol. 78, pp. 2620–2622, 2001.

[22] C. Gmachl, F. Capasso, A. Tredicucci, D. Sivco, A. Hutchinson, and A. Cho, "Long wavelength ($\lambda \simeq 13\mu$m) quantum cascade lasers," *Electron. Lett.*, vol. 34, pp. 1103–1104, 1998.

[23] A. Tredicucci, C. Gmachl, F. Capasso, D. Sivco, A. Hutchinson, and A. Cho, "A multiwavelength semiconductor laser," *Nature*, vol. 396, pp. 350–353, 1998.

[24] G. Strasser, S. Gianordoli, L. Hvozdara, W. Schrenk, K. Unterrainer, and E. Gornik, "GaAs/AlGaAs superlattice quantum cascade lasers at $\lambda \sim 13\mu$m," *Appl. Phys. Lett.*, vol. 75, pp. 1345–1347, 1999.

[25] W. Schrenk, N. Finger, S. Gianordoli, E. Gornik, and G. Strasser, "Continuous-wave operation of distributed feedback AlAs/GaAs superlattice quantum-cascade lasers," *Appl. Phys. Lett.*, vol. 77, pp. 3328–3330, 2000.

[26] L. Wilson, P. Keightley, J. Cockburn, M. Skolnick, J. Clark, R. Grey, and G. Hill, "Controlling the performance of GaAs-AlGaAs quantum-cascade lasers via barrier height modifications," *Appl. Phys. Lett.*, vol. 76, pp. 801–803, 2000.

[27] L. Wilson, J. Cockburn, M. Steer, D. Carder, M. Skolnick, M. Hopkinson, and G. Hill, "Decreasing the emission wavelength of GaAs-AlGaAs quantum cascade lasers by the incorporation of ultrathin InGaAs layers," *Appl. Phys. Lett.*, vol. 78, pp. 413–415, 2001.

[28] S. Gianordoli, W. Schrenk, L. Hvozdara, N. Finger, G. Strasser, and E. Gornik, "Strained InGaAs/AlGaAs/GaAs-quantum cascade lasers," *Appl. Phys. Lett.*, vol. 76, pp. 3361–3363, 2000.

[29] F. Capasso, A. Tredicucci, C. Gmachl, D. Sivco, A. Hutchinson, A. Cho, and G. Scamarcio, "High-performance superlattice quantum cascade lasers," *IEEE J. Select. Topics Quantum Electron.*, vol. 5, pp. 792–807, 1999.

[30] J. Faist, M. Beck, T. Aellen, and E. Gini, "Quantum cascade lasers based on a bound-to-continuum transition," *Appl. Phys. Lett.*, vol. 78, pp. 147–149, 2001.

[31] A. Müller, M. Beck, J. Faist, and U. Oesterle, "Electrically tunable, room-temperature quantum-cascade lasers," *Appl. Phys. Lett.*, vol. 75, pp. 1509–1511, 1999.

[32] S. Blaser, L. Diehl, M. Beck, J. Faist, U. Oesterle, J. Xu, S. Barbieri, and F. Beltram, "Characterization and modeling of quantum cascade lasers based on photon-assisted tunneling transition," *IEEE J. Quantum Electron.*, vol. 37, pp. 448–455, 2001.

[33] D. Hofstetter, J. Faist, M. Beck, A. Müller, and U. Oesterle, " Demonstration of high-performance 10.16 μm quantum cascade distributed feedback lasers fabricated without epitaxial regrowth," *Appl. Phys. Lett.*, vol. 75, pp. 665–667, 1999.

[34] C. Sirtori, F. Capasso, J. Faist, A. Hutchinson, D. Sivco, and A. Cho, "High-temperature operation of distributed feedback quantum-cascade lasers at 5.3 μm,," *IEEE J. Quantum Electron.*, vol. 34, pp. 1722–1729, 1998.

[35] R. Ferreira and G. Bastard, "Evaluation of some scattering times for electrons in unbiased and biased single-and multiple-quantum-well structures," *Phys. Rev. B*, vol. 40, pp. 1074–1086, 1989.

[36] D. Hofstetter, M. Beck, T. Aellen, and J. Faist, "High-temperature operation of distributed feedback quantum-cascade lasers at 5.3 μm," *Appl. Phys. Lett.*, vol. 86, pp. 396–398, 2001.

[37] D. Hofstetter, M. Beck, T. Aellen, J. Faist, U. Oesterle, M. Ilegems, E. Gini, and H. Melchior, "Continuous wave operation of a 9.3 μm quantum cascade laser on a Peltier cooler," *Appl. Phys. Lett.*, vol. 78, pp. 1964–1966, 2001.

[38] D. Hofstetter, J. Faist, M. Beck, and U. Oesterle, "Surface-emitting 10.1 μm quantum-cascade distributed feedback lasers," *Appl. Phys. Lett.*, vol. 75, pp. 3769–3771, 1999.

[39] J. Faist, C. Gmachl, F. Capasso, C. Sirtori, D. Sivco, J. Baillargeon, and A. Cho, "Distributed feedback quantum cascade lasers," *Appl. Phys. Lett.*, vol. 70, pp. 2670–2672, 1997.

[40] M. Troccoli, G. Scamarcio, V. Spagnolo, A. Tredicucci, C. Gmachl, F. Capasso, D. Sivco, A. Cho, and M. Striccoli, "Distributed feedback quantum cascade lasers," *Appl. Phys. Lett.*, vol. 77, pp. 1088–1090, 2000.

[41] P. Kruck, H. Page, C. Sirtori, S. Barbieri, M. Stellmacher, and J. Nagle, "Improved temperature performance of $Al_{0.33}Ga_{0.67}As/GaAs$ quantum-cascade lasers with emission wavelength at $\lambda \sim 11\mu$m,," *Appl. Phys. Lett.*, vol. 76, pp. 3340–3342, 2000.

[42] J. Faist, F. Capasso, C. Sirtori, K. West, and L. Pfeiffer, "Controlling the sign of quantum interference by tunneling from quantum wells," *Nature*, vol. 390, pp. 589–591, 1997.

[43] C. Sirtori, C. Gmachl, F. Capasso, J. Faist, D. Sivco, A. Hutchinson, and A. Cho, " Long-wavelength ($\lambda =$ 8-11.5 μm) semiconductor lasers with waveguides based on surface plasmons," *Opt. Lett.*, vol. 23, pp. 1366–1368, 1998.

[44] N. Mustafa, L. Pesquera, C. Cheung, and K. Stone, "Terahertz bandwidth prediction for amplitude modulation response of unipolar intersubband semiconductor lasers," *IEEE Photon. Technol. Lett.*, vol. 11, pp. 527–529, 1999.

[45] R. Martini, C. Gmachl, J. Falciglia, F. Curti, C. Bethea, F. Capasso, E. Whittaker, R. Paiella, A. Tredicucci, A. Hutchinson, D. Sivco, and A. Cho, "High-speed modulation and free-space optical audio/video transmission using quantum cascade lasers," *Electron. Lett.*, vol. 37, pp. 102–103, 2001.

[46] M. Beck, D. Hofstetter, T. Aellen, J. Faist, U. Oesterle, M. Ilegems, E. Gini, and H. Melchior, "Continuous-wave operation of a mid-infrared semiconductor laser at room-temperature," *Science*, vol. 295, pp. 301–305, 2002.

Jérôme Faist (M'94) was born in Switzerland. He received the Ph.D. degree in physics from the Swiss Institute of Technology, Lausanne, Switzerland, in 1989

He was then with IBM Rueschlikon, Rueschlikon, Switzerland, during 1989–1991 and Bell Laboratories during 1991–1997. In 1997, he became a Full Professor in the Physics Institute of the University of Neuchâtel, Neuchâtel, Switzerland. During his work at Bell Laboratories, he made a key contribution to the invention of the quantum-cascade (QC)laser and to other important milestones such as the first demonstration of continuous-wave operation, the first room-temperature operation, the development of microdisk QC lasers, and distributed feedback QC lasers.

Daniel Hofstetter was born in Zug, Switzerland, in 1966. From 1988 to 1993, he studied physics at the Swiss Federal Institute of Technology (ETHZ), Zurich, Switzerland. In his diploma thesis, he carried out photoacoustic spectroscopy on fatty acids using gas lasers. He received the Ph.D. degree from the Paul Scherrer Institute, Zurich, Switzerland, in 1996, for work which included the design, fabrication, and testing of a semiconductor-based monolithically integrated Michelson interferometer for optical displacement measurement.

After an apprenticeship as an Electrical Mechanic at Landis & Gyr, Zug, Switzerland, during 1982–1986, he became a Physics Technician. He was with XEROX, Palo Alto Research Center, Palo Alto, CA, developing single-mode InGaN-based violet lasers in 1996–1998. In 1998, he joined the group of Jérôme Faist at the University of Neuchâtel, Neuchâtel, Switzerland, where his work concentrated on the fabrication and testing of single-mode distributed-feedback quantum-cascade (QC) lasers and high-performance multimode QC lasers.

Mattias Beck received the M.S. degree in electrical engineering from the Swiss Institute of Technology, Zurich, Switzerland, in 1991, and the Ph.D. degree in physics from the Swiss Institute of Technology, Lausanne, Switzerland, in 1996. His studies focused on the growth and characterization of strained InAlAs–InGaAs–InP heterostructures for high-frequency applications.

He was with Bell Laboratories, Lucent Technologies, Murray Hill, NJ, in 1997, where his work focused on the fabrication of buried heterostructure quantum-cascade (QC) lasers. He joined the Institute of Physics, University of Neuchatel, Neuchâtel, Switzerland, in October 1997, where his work currently focuses on room-temperature continuous-wave operation of QC lasers.

Thierry Aellen was born in La Chaux-de-Fonds, Switzerland, in 1973. He received the M.S. degree in physics from the University of Neuchâtel, Neuchâtel, Switzerland, in 1999, where his hesis focused on ZnSe isolation for quantum-cascade laser (QCL) processing. He is currently working toward the Ph.D. degree at the University of Neuchatel.

His main research interests are distributed-feedback QCLs, high-frequency modulation of QCLs, and QCL reliability.

Michel Rochat was born in Neuchâtel, Switzerland, in 1970. He received the degree in physics from the University of Lausanne, Lausanne, Switzerland, in 1997. He is currently working toward the Ph.D. degree in physics at the University of Neuchâtel, Neuchâtel, Switzerland. His thesis research involves the study of far-infrared intersubband emission from quantum-cascade structures and the realization of a far-infrared laser.

Stéphane Blaser was born in La Chaux-de-Fonds, Switzerland, in 1973. He received the M.S. degree in physics, focused on the visco-elastic response of the mixed state in a ultra-thin film of $YBa_2Cu_3O_7$, in 1997, and the Ph.D. degree in physics in 2002, both from the University of Neuchâtel, Neuchâtel, Switzerland. His studies were focused on the magneto-spectroscopy of intersubband transitions in the mid-to far-infrared region, particularly on quantum-cascade structures based on photon-assisted tunneling transition.